Journal of Pathology
J Pathol November 2021; **255:** 270–284
Published online 25 August 2021 in Wiley Online Library (wileyonlinelibrary.com) DOI: 10.1002/path.5768

ORIGINAL PAPER

Deletion of mTOR in liver epithelial cells enhances hepatic metastasis of colon cancer

Long Jiao[1†‡], Roman Eickhoff[1†], Antje Egners[1], Sandra Jumpertz[1], Johanna Roth[1], Merve Erdem[1], Andreas Kroh[1], Hans Duimel[2], Carmen López-Iglesias[2], Pilar Caro[1$], Lara R Heij[1,3], Maximilian Schmeding[1‖], David Meierhofer[4], Ulf P Neumann[1,5,6,7] and Thorsten Cramer[1,5,8*]

[1] *Department of General, Visceral- and Transplantation Surgery, RWTH University Hospital, Aachen, Germany*
[2] *Microscopy Core Lab, FHML and M4I Maastricht Multimodal Molecular Imaging Institute, Maastricht University, Maastricht, The Netherlands*
[3] *Pathology, RWTH University Hospital, Aachen, Germany*
[4] *Max Planck Institute for Molecular Genetics, Berlin, Germany*
[5] *ESCAM – European Surgery Center Aachen Maastricht, Aachen, Germany*
[6] *ESCAM – European Surgery Center Aachen Maastricht, Maastricht, The Netherlands*
[7] *Department of Surgery, Maastricht University Medical Center, Maastricht, The Netherlands*
[8] *NUTRIM School of Nutrition and Translational Research in Metabolism, Maastricht University, Maastricht, The Netherlands*

**Correspondence to: T Cramer, Molecular Tumor Biology, General, Visceral- and Transplantation Surgery, University Hospital RWTH Aachen, Pauwelsstraße 30, 52074 Aachen, Germany. E-mail: tcramer@ukaachen.de*

[†]These authors contributed equally.
[‡]Department of General Surgery, The First Affiliated Hospital of Nanchang University, Nanchang, PR China
[$]Institute of Human Genetics, Heidelberg University Hospital, Heidelberg, Germany
[‖]Department of Surgery, Klinikum Dortmund, Dortmund, Germany

Abstract

Activation of the mechanistic target of rapamycin (mTOR) pathway is frequently found in cancer, but mTOR inhibitors have thus far failed to demonstrate significant antiproliferative efficacy in the majority of cancer types. Besides cancer cell-intrinsic resistance mechanisms, it is conceivable that mTOR inhibitors impact on non-malignant host cells in a manner that ultimately supports resistance of cancer cells. Against this background, we sought to analyze the functional consequences of mTOR inhibition in hepatocytes for the growth of metastatic colon cancer. To this end, we established liver epithelial cell (LEC)-specific knockout (KO) of mTOR ($mTOR^{LEC}$) mice. We used these mice to characterize the growth of colorectal liver metastases with or without partial hepatectomy to model different clinical settings. Although the LEC-specific loss of mTOR remained without effect on metastasis growth in intact liver, partial liver resection resulted in the formation of larger metastases in $mTOR^{LEC}$ mice compared with wildtype controls. This was accompanied by significantly enhanced inflammatory activity in LEC-specific mTOR KO livers after partial liver resection. Analysis of NF-κB target gene expression and immunohistochemistry of p65 displayed a significant activation of NF-κB in $mTOR^{LEC}$ mice, suggesting a functional importance of this pathway for the observed inflammatory phenotype. Taken together, we show an unexpected acceleration of liver metastases upon deletion of mTOR in LECs. Our results support the notion that non-malignant host cells can contribute to resistance against mTOR inhibitors and encourage testing whether anti-inflammatory drugs are able to improve the efficacy of mTOR inhibitors for cancer therapy.

Keywords: liver metastasis; colon cancer; mTOR; NF-κB; inflammation; necroptosis; liver regeneration

Received 24 September 2020; Revised 2 July 2021; Accepted 21 July 2021

No conflicts of interest were declared.

Introduction

Colorectal cancer (CRC) ranks as the third most frequent malignant tumor worldwide and is accompanied by substantial cancer-associated morbidity and mortality [1]. Although the prognosis of patients with locally confined tumor growth has improved significantly in recent years [2], clinical care of metastasized CRC remains challenging [3]. Due to the continuous development of surgical techniques and the establishment of interdisciplinary therapy planning, CRC patients with liver metastases can now undergo treatment with curative intent [4]. This is an impressive achievement and about 25% of patients survive 5 years or longer [4]. Unfortunately, the majority of patients still develop tumor recurrence in the liver or other organs and ultimately succumb to

the disease [2]. This demonstrates the urgent need to better understand the pathogenesis of both primary and secondary liver metastasis in CRC.

Our understanding of the molecular and cell biological mechanisms that govern the function of non-tumor cells for organ metastasis has greatly improved in recent years. The vast majority of publications have focused on the role of immune cells, fibroblasts and endothelial cells of the tumor microenvironment for metastatic niche formation [5]. Rather astonishingly, the function of hepatocytes, by far the most abundant cell type in the liver, for hepatic metastasis received a lot less attention. It was reported over 30 years ago that specific lectins on hepatocytes are functionally important for liver metastasis via mediating adherence of tumor cells to the liver [6]. Shortly thereafter, Brodt's group [7] showed paracrine stimulation of metastatic cell growth by IGF-1 secreted from hepatocytes. It was not until recently, however, that the mechanistic importance of hepatocytes for directing metastatic niche formation has received substantially more attention. A very elegant study directed by Beatty [8] has shown that IL-6 (derived from the microenvironments of pancreas and colon cancer) stimulates hepatocytes to release serum amyloid A (and other factors) to induce the accumulation of myeloid cells and the activation of hepatic stellate cells, thereby supporting metastatic seeding and outgrowth. With an equally impressive experimental approach, Halder and colleagues [9] were able to show that both primary and secondary liver tumors resulted in activation of the Hippo downstream effectors YAP and TAZ in hepatocytes and that experimental hyperactivation of YAP in hepatocytes surrounding melanoma-derived liver metastasis inhibited tumor growth. These studies convincingly demonstrated that hepatocytes are able to support as well as constrain metastatic progression in the liver and they underscore the need to better understand the pathways involved.

Metabolic reprogramming is a hallmark of both primary tumor formation and metastasis [10]. Besides cellular growth, antioxidant defense and therapy resistance, tumor-specific metabolic alterations are of pivotal importance for various stages of metastasis [11]. Although cancer metabolism was for the longest time thought to be primarily determined by cell-intrinsic factors, e.g. genetic changes, we now know that the tumor microenvironment is able to profoundly modify the metabolic activity of cancer cells [12]. Breast cancer cells, for example, display significant differences in their use of anaplerotic pathways between primary tumor and lung metastases, suggesting a causal involvement of the tumor microenvironment [13]. With respect to colon cancer, it was shown that creatine in the extracellular space of the liver is used by cancer cells for ATP generation, ultimately facilitating the survival and growth of hepatic metastasis [14]. These fascinating results led us to hypothesize that intervening with the metabolism of hepatocytes could inhibit the survival of colon cancer metastases in the liver, potentially representing a novel therapeutic approach. To test our hypothesis, we evaluated the consequences of a functional loss of the mechanistic target of rapamycin (mTOR) pathway in hepatocytes. The highly conserved serine/threonine kinase mTOR translates nutrient availability and growth factor signaling into different cellular responses [15]. Under conditions of abundant nutrients (e.g. glucose and amino acids), growth and proliferation of cells is encouraged by mTOR [16]. Conversely, when nutrients are scarce, mTOR signaling is inhibited, resulting in a reduction of anabolic processes (e.g. protein and lipid synthesis), induction of autophagy, and, ultimately, cessation of cellular proliferation [17]. mTOR consists of two functionally and molecularly distinct complexes: mTOR complex 1 (mTORC1) is activated by nutrients and growth factor signaling and inhibited by rapamycin, whereas mTOR complex 2 (mTORC2) is mainly activated by growth factors and is insensitive towards acute rapamycin treatment [15]. Taken together, mTOR is considered to be a central signaling relay for the orchestration of cellular metabolism with environmental conditions. The mTOR pathway is considered to be an attractive target for cancer therapy and numerous agents with mTOR inhibitory functions are currently either approved or being developed further. Unfortunately, suboptimal clinical efficacy due to secondary resistance is a common event during antiproliferative therapy with mTOR inhibitors. In addition, genetic loss of mTOR can result in aggravation of tumor formation, as has been shown for a murine model of primary liver tumorigenesis [18]. Against this background it is of pivotal importance to better understand the consequences of cell type-specific mTOR inhibition in the context of cancer.

Materials and methods

Animal experiments

All experiments were carried out in accordance with the German legislation governing animal studies and the Guide for the Care and Use of Laboratory Animals (National Institutes of Health, Publication no. 85-23, revised 2011). The experiments were approved by the Governmental Animal Care and Use Committee [Landesamt für Natur Umwelt und Verbraucherschutz (LANUV) Nordrhein-Westfalen, Recklinghausen, Germany; reference number: 84-02.04.2015.A126 and 81-02.04.2017.A398]. Liver epithelial cell (LEC)-specific mTOR knockout (KO) mice (termed $mTOR^{LEC}$) were generated using the Cre/loxP system [19] with floxed mTOR mice [20] and albumin-Cre mice [21]. Mice aged 8–12 weeks were used for the experiments. The mice were housed in the Institute for Laboratory Animal Science at the University Hospital of the RWTH Aachen University. Mice were given *ad libitum* access to water and chow in a gas-tight room under strict 12 h light/dark cycles (day: 7:00 am-7:00 pm), with H_2O_2 gas-disinfection, cage bedding, 22 ± 1 °C room temperature, 50 ± 10% relative humidity and specific pathogen-free conditions.

Antibodies

Phospho-Akt (Ser473) [Cell Signaling Technology, Frankfurt, Germany, #4060, dilution 1:1000 for western blot (WB)], β-actin (Sigma-Aldrich, Taufkirchen, Germany, #A5441, dilution 1:1000 for WB), cleaved caspase-3 [Cell Signaling Technology, #9661, dilution 1:200 for immunohistochemistry (IHC)], CD45 (Thermo Fisher Scientific, Waltham, MA, USA, #14-0451-82, dilution 1:100 for IHC), F4/80 (Thermo Fisher Scientific, #14-4801-82, dilution 1:200 for IHC), Ki-67 (Cell Signaling Technology, #12202, dilution 1:200 for IHC), Ly-6G (BioLegend, San Diego, CA, USA, #127601, dilution 1:200 for IHC), LC3B (Sigma-Aldrich, #L7543, dilution 1:1000 for WB), mTOR (Cell Signaling Technology, #2983, dilution 1:1000 for WB), p62 (SQSTM1) (MBL International, Woburn, MA, USA, #PM045, dilution 1:500 for WB), p65 (Cell Signaling Technology, #8242, dilution 1:100 for IHC), p-p70-S6 kinase (Cell Signaling Technology, #9234, dilution 1:1000 for WB), p-histone H3 (Cell Signaling Technology, #9701, dilution 1:200 for IHC), RIP3 (Prosci, Fort Collins, CO, USA, #2283, dilution 1:1000 for WB), GAPDH (Cell Signaling Technology, #5174, dilution 1:1000 for WB), GP73 (Santa Cruz, Heidelberg, Germany, #sc-48 011, dilution 1:200 for IHC).

Cell lines and primary hepatocytes

The established murine colon carcinoma cell line MC38 [22] was maintained in DMEM Ham's Nutrient Mixture F-12 (Sigma-Aldrich, D8437) with 10% FBS (Gibco/Thermo Fisher Scientific). Cells were used between passages 10 and 25 at approximately 70–90% confluence. Primary murine hepatocytes were isolated from livers of wildtype (WT) and $mTOR^{LEC}$ mice at 8–12 weeks of age and maintained in DMEM with 10% FBS as previously reported [23]. Cells were cultured in a humidified incubator with 5% CO_2 at 37 °C.

Mouse model of CRC liver metastasis

All surgical procedures were performed under general anesthesia. Analgesia was ensured by buprenorphine (0.05 mg/kg BW) 30 min before skin incision and in 8 h intervals for 3 days after the operation. Anesthesia was performed with an isoflurane-oxygen mixture (induction: 3–4% isoflurane; maintenance: 1–1.5% isoflurane; oxygen flow 2 l/min), and mice were fixed in a supine position on a heating pad. The abdominal cavity was exposed through a 3-cm midline laparotomy and an abdominal wall retractor system was placed. The spleen was exposed on a gauze and 7.5×10^4 MC38 cells in 250 µl HBSS (Gibco/Thermo Fisher Scientific) were injected into the central part of the spleen within 15 s; the needle was maintained in the spleen for 2 min. Afterwards, the spleen was removed, and the abdominal wall was closed by suturing the muscle layer followed by the skin. After 14 days, the mice were anesthetized as described previously and the abdominal cavity was reopened. The left-anterior and right-anterior segments of the liver including the gallbladder were resected by hemostatic clip ligation according to published literature [24]. After establishing hemostasis, the abdominal cavity was closed and analgesia was continued for 3 days. All mice were sacrificed 4 weeks after the initial operation and the number of metastatic nodules was evaluated. To ensure that the observed hepatic tumor nodules were not of hepatocellular origin, IHC for GP73, a well-established marker for hepatocellular carcinoma, was performed (see supplementary material, Figure S1).

Isolation of genomic DNA and total RNA and RT-qPCR analyses

Genomic DNA was isolated from mouse ear punches and hepatocytes with a NucleoSpin Tissue Kit (Macherey-Nagel, Düren, Germany). RNA was isolated from mouse liver using peqGOLD RNAPure reagent (VWR, Langenfeld, Germany) and QIAshredder spin columns (Qiagen, Hilden, Germany) according to the manufacturers' instructions. RNA yield and purity were determined spectrophotometrically. RNA integrity was checked by MOPS-buffered denaturing RNA gel electrophoresis and only samples with a 28S/18S ratio of at least 1.8 were included in the RT-qPCR study. First strand cDNA of 1 µg total RNA per reaction was synthesized with an oligo (dT) primer and a SuperScript™ First Strand Synthesis System (Invitrogen/Thermo Fisher Scientific). Quantitative real-time PCR analysis was conducted on an ABI 7500 Real-Time PCR system using PowerSYBR® Green PCR Master Mix (Thermo Fisher Scientific). Primer-specific annealing temperatures were pre-evaluated prior to the study to optimize PCR conditions. Primer specificity was checked by melt curve analyses and Tris-acetate-EDTA (TAE)-buffered DNA agarose gel electrophoresis of obtained PCR products. Amplification efficiency was calculated with LinRegPCR 2016.0 (Heart Failure Research Center, Amsterdam, the Netherlands) and used for efficiency corrections [25]. Inter-Run calibrators were used if necessary to correct for inter-run variations. Relative fold-changes of target gene expression were calculated with qbase+ 3.0 (Biogazelle, Zwijnaarde, Belgium) that automatically applies the abovementioned corrections to the ΔΔCq method [26]. Primer sequences are shown in supplementary material, Table S1.

Protein isolation and WB analyses

Hepatocytes or liver tissue samples were lysed in RIPA lysis buffer (10 mM Tris–HCl pH 7.5, 150 mM sodium chloride, 0.25% SDS, 10 mg/ml sodium deoxycholate, 1% Nonidet P40, 1 mM Na_3VO_4, 1 mM DTT, 2 mM PMSF, 10 mM sodium fluoride, 2 µM leupeptin, and 4.4×10^{-4} TIU/mg aprotinin). The lysate was sonicated and clarified by centrifugation ($12\,000 \times g$, 10 min, 4 °C), snap frozen in liquid nitrogen and stored at −80 °C until assayed. Total protein samples (30 µg) were heated at 95 °C for 5 min in sample buffer,

subjected to PAGE and electro-transferred on to nitrocellulose membranes (GE Healthcare, Solingen, Germany). Blocking with 5% non-fat dry milk or BSA (Carl Roth, Karlsruhe, Germany) was for 1 h at room temperature. Blocking buffer was removed and the membranes were incubated with the primary antibody overnight at 4 °C. After washing three times for 5 min in TBST (TBS buffer with 0.1% v/v Tween-20), the secondary antibody was applied for 1 h at room temperature. Thereafter, the membrane was washed three times for 5 min with TBST, incubated for 1 min with ECL reagents (Perkin Elmer, Waltham, MA, USA) and the signal was captured using an INTAS ECL Chemocam imager (INTAS Science Imaging, Göttingen, Germany).

Immunohistochemistry

All IHC experiments were performed on formalin-fixed, paraffin-embedded tissues with heat-mediated antigen retrieval [10 min at 110 °C in Dako Target Retrieval Solution pH6 in a Decloaking Chamber (Biocare Medical, Pacheco, CA, USA)]. After washing twice with TBST, the slides were treated with blocking buffer (ZytoChem Plus AP kit, Zytomed Systems, Bargteheide, Germany) for 5 min, followed by avidin and biotin blocking for 15 min (Avidin/Biotin Blocking Kit, Vector Labs, Burlingame, CA, USA). Slides were incubated with primary antibody overnight at 4 °C, followed by two washing steps and application of the secondary antibody for 1 h at room termperature. After repeated washing with TBST, a streptavidin-AP conjugate [ZytoChem Plus alkaline phosphatase (AP) kit, Zytomed Systems] was applied for 15 min at room temperature and a color reaction developed using AP red solution (Permanent AP Red Kit, Zytomed Systems). The reaction was stopped by washing the slides briefly in demineralized water and nuclei were counterstained with hematoxylin.

Oil Red O staining

Cryosections were cut at 10 µm and immediately fixed in ice-cold formalin for 10 min. After washing with PBS for 5 min, sections were incubated in 60% propan-2-ol for 10 s. The Oil Red O staining solution was applied for 15 min, followed by running tap water for 5 min; nuclei were stained briefly with hematoxylin for 30 s. The reaction was stopped in demineralized water and slides were mounted using glycerol gelatin (Glycergel, Dako/Agilent, Santa Clara, CA, USA) and coverslipped.

Electron microscopy

Liver tissue of WT and $mTOR^{LEC}$ mice was fixed with 1.5% glutaraldehyde in 0.067 M cacodylate buffer at pH 7.4 containing 1% sucrose and kept in the fixative for 24 h at 4 °C. Then, tissue samples were washed with 0.1 M cacodylate buffer with sucrose and post-fixed with 1% osmium tetroxide in the same buffer containing 1.5% potassium ferricyanide for 1 h at 4 °C. Samples were then washed in 0.1 M cacodylate followed by dehydration in ethanol, infiltration with Epon resin for 48 h, embedding in the same resin, and polymerization at 60 °C for 48 h. Ultrathin sections were obtained using a Leica Ultracut UCT ultramicrotome and mounting on Formvar-coated copper grids. These were stained with 2% uranyl acetate in water and lead citrate. Finally, sections were analyzed in a Tecnai T12 electron microscope equipped with an Eagle 4kx4k CCD camera (Thermo Fisher Scientific).

Proteomics sample preparation with label-free quantification

Approximately 10 mg frozen liver tissue per sample was homogenized three times for 60 s ($4\ m \times s^{-1}$) under denaturing conditions (in 1 ml of a buffer containing 4% SDS, 0.1 M DTT, 0.1 M Tris pH 7.8), followed by sonication for 1 min, heating at 95 °C for 5 min in a thermal shaker, and centrifuged at 15 000 × *g* for 5 min. Each supernatant was transferred into a new low protein binding tube (Eppendorf, Hamburg, Germany). Protein precipitation was achieved by adding four times excess volume of ice-cold acetone at −20 °C overnight. Pelleting at maximum speed at 4 °C was followed by three washes with acetone and samples were dried in a vacuum concentrator. Lyophilized proteins were dissolved in 6 M guanidinium chloride, 5 mM tris(2-carboxyethyl)phosphine, 20 mM chloroacetamide and 50 mM Tris–HCl pH 8.5. Samples were heated for 5 min at 95 °C and sonicated for 15 min in a water bath sonicator. About 150 µg protein per sample (~10 µl) were diluted 1:10 with nine volumes of 10% acetonitrile and 25 mM Tris pH 8.5, then trypsin digested (1:50) at 37 °C overnight. The resulting peptides were purified using C18 columns and further fractionated by strong cation exchange (3 M Purification, Meriden, CT, USA) chromatography. Desalted peptides were dissolved in 0.1% formic acid in water and further separated into four fractions using strong cation exchange. Eluates were first dried in a SpeedVac, then dissolved in 10 µl 5% acetonitrile and 2% formic acid in water, briefly vortexed, then sonicated in a water bath for 30 s prior to injection into a nano-liquid chromatography with tandem mass spectrometry (nano-LC–MS/MS). Five micrograms of each strong cation exchange fraction and a non-fractioned sample were used for proteome profiling.

LC–MS/MS instrument settings for shotgun proteome profiling and data analysis

LC–MS/MS was carried out by nanoflow reverse-phase LC (Dionex Ultimate 3000, Thermo Scientific) coupled online to a Q-Exactive Plus Orbitrap MS (Thermo Fisher Scientific). In brief, the LC separation was carried out using a PicoFrit analytical column (75 µm ID × 55 cm long, 15 µm Tip ID; New Objectives, Woburn, MA, USA) in-house packed with 2.1 µm C18 resin

(Reprosil-AQ Pur, Dr. Maisch, Ammerbuch, Germany). Peptides were eluted using a non-linear gradient from 3.8 to 50% solvent B over 173 min at a flow rate of 266 nl/min (solvent A: 99.9% water, 0.1% formic acid; solvent B: 79.9% acetonitrile, 20% water, 0.1% formic acid). 3.5 kV were applied for nanoelectrospray ionization. A cycle of one full Fourier transform (FT) scan mass spectrum (300–1750 m/z, resolution of 70 000 at m/z 200, AGC target 1×10^6) was followed by 12 data-dependent MS/MS scans (200–2000 m/z, resolution of 35 000, AGC target 5×10^5, isolation window 2 m/z) with normalized collision energy of 25 eV. Target ions already selected for MS/MS were dynamically excluded for 30 s. In addition, only peptide charge states between two and eight were allowed. Raw MS data were processed with MaxQuant software (v1.6.10.43, Max-Planck-Institut für Biochemie, Martinsried, Germany) and searched against the murine proteome database UniProtKB with 55 153 entries, released in August 2019. Parameters for the MaxQuant database search were: a false discovery rate (FDR) of 0.01 for proteins and peptides, a minimum peptide length of seven amino acids, a first search mass tolerance for peptides of 20 ppm and a main search tolerance of 4.5 ppm, and using the function 'match between runs'. A maximum of two missed cleavages was allowed for the tryptic digest. Cysteine carbamidomethylation was set as a fixed modification, whereas N-terminal acetylation and methionine oxidation were set as variable modifications. Contaminants, as well as proteins identified by site modification and proteins derived from the reversed part of the decoy database, were strictly excluded from further analysis. The MS data have been deposited with the ProteomeXchange Consortium (http://proteomecentral.proteomexchange.org) via the PRIDE partner repository [27] with the dataset identifier PXD019998.

Experimental design, statistical rationale, pathway, and data analyses

The correlation analysis of biological replicates and the calculation of significantly different proteins was carried out with Perseus (v1.6.10.43, Max-Planck-Institut für Biochemie). Label-free quantification intensities, originating from at least two different peptides per protein group, were transformed by log2. Only protein groups with valid values within compared experiments were used for further data evaluation. Statistical analysis was carried out by a two-sample *t*-test with Benjamini-Hochberg (FDR 0.05) correction for multiple testing. For comprehensive proteome data analyses, we applied gene set enrichment analysis (v3.0) [28] in order to determine if *a priori* defined sets of proteins show statistically significant, concordant differences between KO and controls. We used gene set enrichment analysis standard settings, except that the minimum size exclusion was set to 5 and Reactome v7.0 and KEGG v7.0 were used as gene set databases. The cut-offs for significantly regulated pathways were set at $p \leq 0.05$ and FDR ≤ 0.25.

Results

Basic characterization of mTOR^{LEC} KO mice

To investigate the functional role of mTOR in hepatocytes for liver metastasis, we generated mTOR^{LEC} mice via the Cre/loxP system [19]. Quantitative PCR with genomic DNA isolated from primary hepatocytes displayed a deletion efficiency of approximately 50% (see supplementary material, Figure S2A). WB analysis of primary hepatocytes isolated from mTOR^{LEC} mice revealed a strong reduction of the mTOR protein, whereas whole liver lysates failed to show a significant difference between WT and mTOR^{LEC} mice (see supplementary material, Figure S2B). To analyze the functional effects of the mTOR loss, established downstream target proteins of mTOR were characterized via immunoblot. As shown in supplementary material, Figure S2C, both basal and stimulated phosphorylation of p70/S6K is clearly reduced in mTOR-deficient hepatocytes. Insulin-stimulated activation of Akt was enhanced in KO hepatocytes, in line with an earlier report investigating mTOR-deficient adipocytes [29]. Overall, these results demonstrated sufficient inhibition of the mTOR signaling pathway in mTOR^{LEC} mice. To characterize the effect of the LEC-specific mTOR loss on the global proteome, label-free MS was carried out. Pearson correlation was used to compare the proteome profiles of all five biological replicates of WT and mTOR^{LEC} mice. The Pearson correlation coefficients determined for all replicates of WT and KO liver tissue proteomics ranged between 0.926 and 0.99 (see supplementary material, Figure S3A), indicative of high reproducibility. A volcano plot visualized proteins with significantly different expression between the genotypes (see supplementary material, Figure S3B and Table 1). With the help of the Search Tool for the Retrieval of Interacting Genes/Proteins (STRING) software, the network of molecular interactions among downregulated proteins (at least one SD from the mean) was visualized (see supplementary material, Figure S4). The most striking and significantly downregulated pathways within this network were RNA binding (FDR: 3.62e-09, GO) and the ribosome (FDR: 1.03e−05, KEGG), both known to be under the control of the mTOR pathway, further supporting functional mTOR inactivation [30]. Taken together, the LEC-specific loss of mTOR had only modest effects on the proteome profile, which can be explained either by insufficient KO efficiency or by activation of compensatory pathways. Next, we sought to evaluate the impact of the LEC-specific mTOR loss on liver histology. Various routine histochemical stains (H&E, Sirius red, and Oil Red O) did not show significant differences between WT and mTOR^{LEC} mice other than greater size of hepatocytes in KO livers (Figure 1 and supplementary material, Figure S5). Furthermore, hepatocellular proliferation (judged by Ki-67 nuclear positivity; see supplementary material, Figure S6) and apoptosis (using cleaved caspase-3; see supplementary material, Figure S6) were not different between the

Table 1. List of significantly altered proteins in mTOR^{LEC}/WT liver tissue. Posterior error probability (PEP), MS2 spectral count frequency (MS/MS count), Benjamini–Hochberg corrected *P* values and fold-changes are shown.

Protein names	Gene symbol	MS/MS count	-LOG *t*-test *P* value	Fold-change KO/WT
3 beta-hydroxysteroid dehydrogenase type 5;3 beta-hydroxysteroid dehydrogenase type 4	Hsd3b5	81	3.4671	0.21
Gap junction beta-1 protein	Gjb1	14	2.9446	0.31
Cytochrome P450 4A12A	Cyp4a12a	115	2.6623	0.36
Cytochrome P450 2F2	Cyp2f2	95	2.8650	0.39
Proteasome subunit alpha type-7	Psma7	224	2.8286	0.47
Arginyl-tRNA-protein transferase 1	Ate1	31	3.5517	0.59
Putative ataxin-7-like protein 3B	Atxn7l3b	25	3.5199	2.29
Cyclic AMP-responsive element-binding protein 1	Creb1	51	2.7910	3.80
Stathmin	Stmn1	133	2.4677	4.40
Small EDRK-rich factor 2	Serf2	11	2.7473	4.42

genotypes. Given the importance of hepatocytes for hepatic macrophages [31], we sought to characterize the effect of the LEC-specific mTOR loss on the abundance of inflammatory cells in the liver. Although the number of total leukocytes (visualized by CD45 IHC) was unchanged, significantly higher numbers of F4/80-positive macrophages were detected in mTOR^{LEC} mice (Figure 2). As treatment of myeloid cells with rapamycin, a well-established inhibitor of mTORC1, promotes the secretion of proinflammatory factors (e.g. TNF-α and IL-6) [32–34], we determined the expression of genes known to impact on the recruitment of inflammatory cells. As can be seen in supplementary material, Figure S7, IL-1β *(Il1b)*, TNF-α (*Tnfa)*, CCL2 *(Ccl2)*, macrophage migration inhibitory factor *(Mif)*, TGF-β1 *(Tgfb1)*, IL-6 (*Il6)*, C-reactive protein (*Crp*) and the anti-inflammatory cytokine IL-10 *(Il10)* were expressed at similar levels in the livers of WT and mTOR^{LEC} mice. Autophagy, a catabolic process affecting organelle degradation and protein turnover [35], is of central importance for liver biology and is inhibited by mTOR [36,37], suggesting that autophagy might be enhanced in mTOR^{LEC} mice. However, analysis of autophagy based on the detection of LC3B processing, p62 protein expression, and electron microscopy-based visualization of autophagosomes could not detect significant differences between the livers of WT and mTOR^{LEC} mice (see supplementary material, Figure S8). In summary, with the exception of enhanced macrophage abundance in KO livers, the LEC-specific functional inactivation of mTOR remained without significant effects on the majority of basic biological and histological traits.

Liver metastasis of colon cancer cells is not affected by LEC-specific loss of mTOR

Liver metastases of colon cancer in mice were established according to an established protocol [38]. Injection of the established murine colon cancer cell line MC38 [22] into the spleen (with subsequent splenectomy) resulted in the formation of visible liver metastasis after 28 days (Figure 3A). Quantification of the metastatic load revealed no difference between WT and mTOR^{LEC} mice (Figure 3A). In line with this result, the relative number of proliferating cells, both in the benign liver adjacent to the metastases and in the tumor nodules themselves, were similar between the genotypes (see supplementary material, Figure S9). IHC was applied to characterize the inflammatory reaction of the liver surrounding the metastatic nodules. Neutrophils (Ly6G) displayed no significant difference when WT and mTOR^{LEC} mice were compared (Figure 3B). Of note, the abundance of total leukocytes (CD45) and F4/80-positive macrophages was significantly higher upon LEC-specific loss of mTOR (Figure 3B), reminiscent of the findings in unchallenged mice (Figure 2).

Loss of mTOR in LECs enhances liver metastasis after partial hepatectomy

To be able to mirror the clinical situation of surgical resection of liver metastases, we performed partial liver resection 14 days after injection of the murine colon cancer cell line into the spleen (see supplementary material, Figure S10). This resulted in a clear acceleration of metastasis progression in the mTOR^{LEC} mice (Figure 4A). Analysis of the proliferation of metastasis-adjacent liver cells and tumor cells again showed no difference between WT and mTOR^{LEC} mice (see supplementary material, Figure S11). Of note, the inflammatory activity in the benign liver surrounding the metastatic nodules was significantly enhanced in mice harboring a LEC-specific mTOR deletion. All examined cell types (total leukocytes, F4/80-positive macrophages, and neutrophils) were found at significantly higher levels in mTOR^{LEC} compared with WT mice (Figure 4B). We sought to better understand the underlying mechanism and decided to analyze NF-kB activity, as this pathway is both crucial for the inflammatory response [39] and has been shown to functionally interact with mTOR [32,40]. IHC-based determination of p65 localization demonstrated strongly enhanced nuclear positivity in hepatocytes in mTOR^{LEC} compared with WT mice (Figure 5A and supplementary material, Figure S12). Furthermore, various established NF-kB target genes with proinflammatory functions (*Il1b, Tnfa*, *Ccl2*, *Ccl5*, *Cxcl1*, *Cxcl2*, and *Cxcl5*) were expressed at significantly higher levels in the livers of

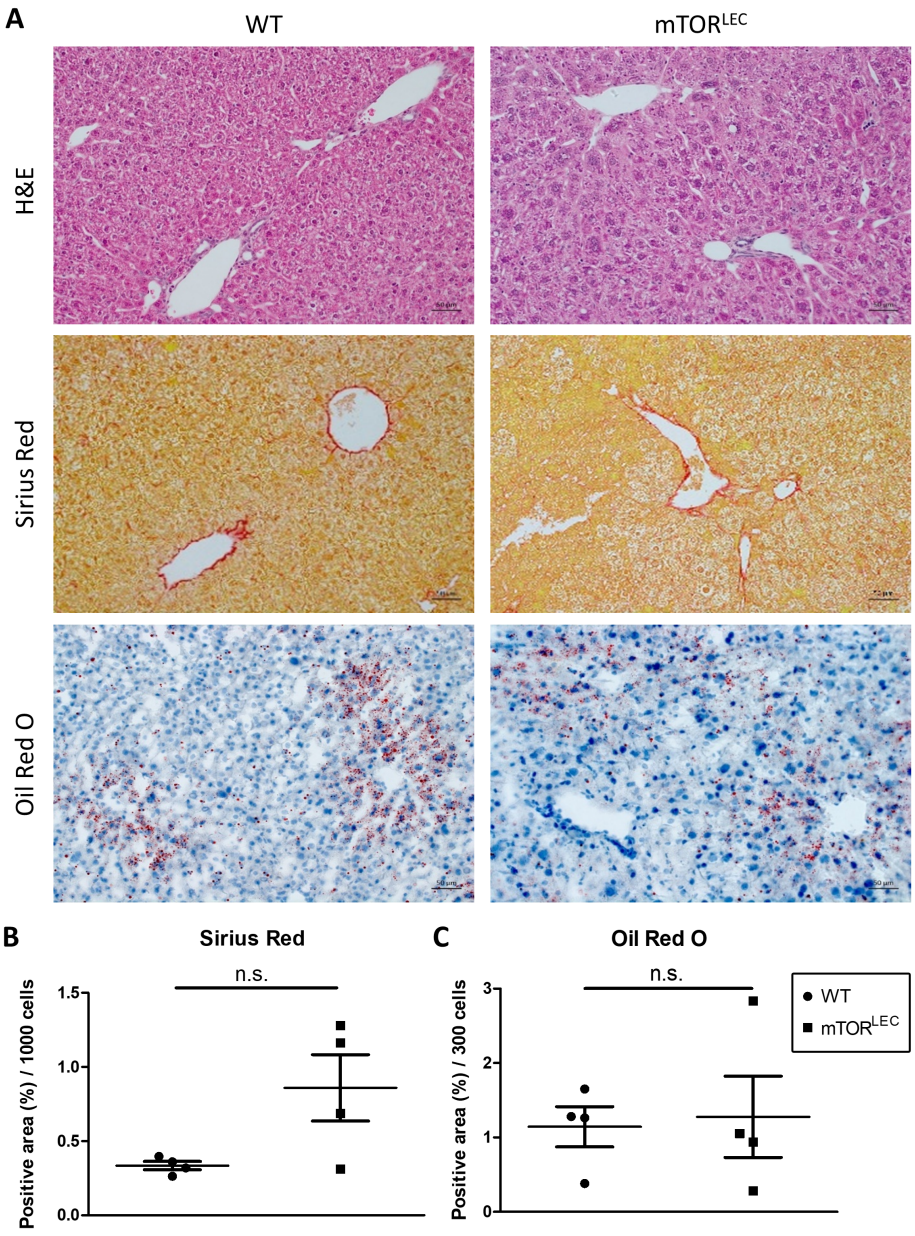

Figure 1. Basic histopathological traits are not affected by the LEC-specific mTOR loss. (A) Liver sections from WT and mTOR^{LEC} mice were stained with H&E, Sirius Red, and Oil Red O; scale bar = 50 µm. (B, C) Positive areas were quantified with ImageJ software, normalized to number of cells per field of view and shown as bar charts. Mean ± SEM, statistically analyzed using unpaired two-sided Student's *t*-test.

mTOR^{LEC} KO mice (Figure 5B). These results suggested that the loss of mTOR in liver parenchymal cells aggravated the growth of colon cancer liver metastases via NF-kB-mediated inflammation.

Partial hepatectomy results in necroptosis upon LEC-specific deletion of mTOR

The histopathological analysis of the tissue samples demonstrated the existence of focal necrotic areas exclusively in the livers of mTOR^{LEC} mice after partial liver resection (Figure 6A and supplementary material, Figure S13). As these areas morphologically resembled necroptosis [41,42], we decided to analyze the protein expression of the established necroptosis marker protein kinase receptor-interacting protein 3 (RIP3K) [43]. Indeed, RIP3K was found to be stabilized in the livers of mTOR^{LEC} mice after partial hepatectomy (Figure 6B), supporting the emergence of necroptosis in this setting. IHC displayed a robust inflammatory response to the focal necrotic areas (Figure 6A), in line with the established proinflammatory consequences of necroptosis [44].

Discussion

Our results demonstrate that inhibiting the mTOR kinase in LECs aggravates metastatic growth of colon cancer after partial liver resection. This is especially intriguing as the Cre/loxP-mediated efficacy of mTOR inhibition

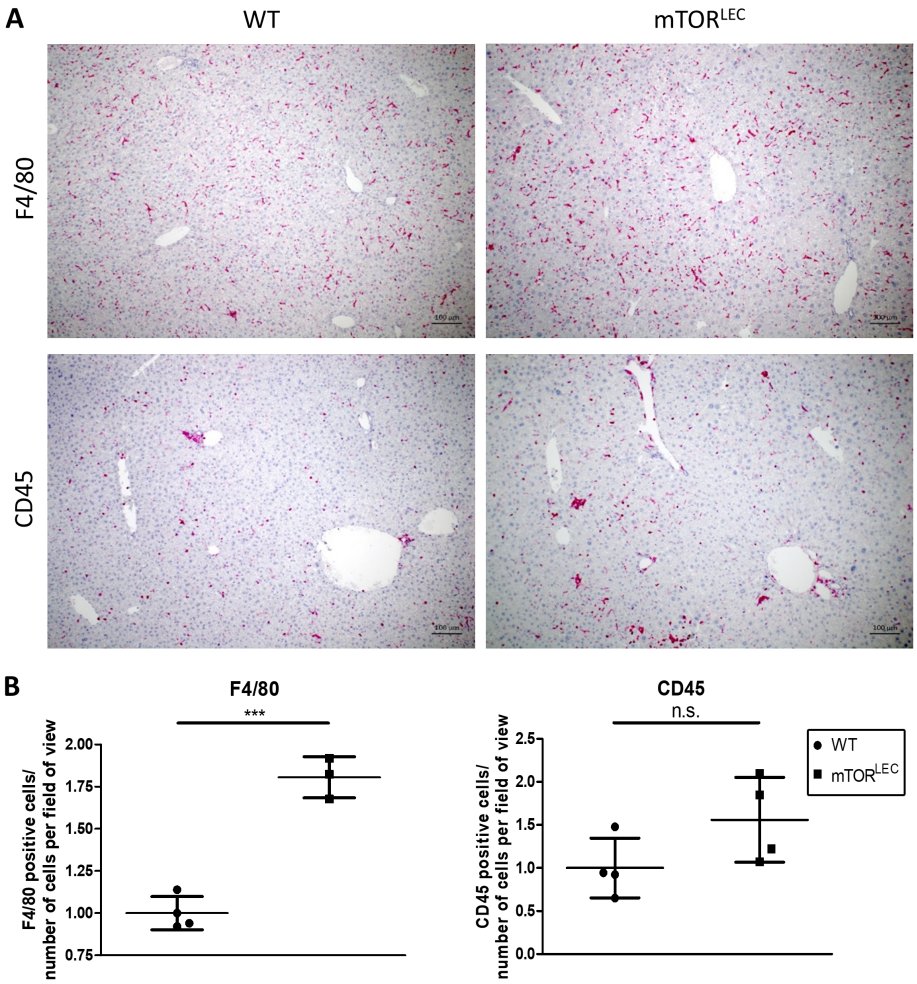

Figure 2. LEC-specific mTOR deletion results in elevated numbers of F4/80+ macrophages in the liver. (A) IHC for F4/80 and CD45 in liver sections from WT and $mTOR^{LEC}$ mice (scale bar = 100 μm). (B) Positive cells were counted using ImageJ software, normalized to number of cells per field of view and shown as bar charts. Mean ± SEM, statistically analyzed using unpaired two-sided Student's *t*-test, $^{***}p < 0.001$.

was limited to approximately 50% in our experiments (on the level of genomic DNA; see supplementary material, Figure S1A). Unfortunately, two earlier reports that examined mice with albumin-Cre-directed inactivation of mTOR did not state the deletion efficacy [45,46], precluding the comparison of our results with the published literature. However, our results are comparable with published data from the group of Sabatini, demonstrating for the first time that mice with a partial mTOR KO (mice carrying only a single *Mtor* copy) constitute valid experimental tools [47].

We observed elevated inflammatory activity in the livers of $mTOR^{LEC}$ mice after partial hepatectomy and provide experimental evidence to support a functional role of canonical NF-κB in this setting. These results are in line with data from $mTOR^{LEC}$ mice after hepatic ischemia/reperfusion injury [45] and clinical experience with mTOR inhibitors as rapamycin and its derivatives are known to induce both systemic and organ-specific (e.g. lung, skin, kidney, intestine) inflammation [48,49]. In addition, LEC-specific loss of mTORC1 (via deletion of the regulatory subunit Raptor) resulted in enhanced hepatic inflammation, characterized by elevated numbers of macrophages as well as T- and B-lymphocytes [50]. A functional interdependence of mTOR and NF-κB signaling was reported for the first time by the group of Hunter, noting attenuated NF-κB activity upon activation of mTORC1 (via deletion of the negative mTORC1 regulators TSC1 and TSC2) [40]. Shortly thereafter, researchers from Vienna not only confirmed the attenuating function of mTORC1 activation but went on to show that mTORC1 inhibition (via rapamycin) actually enhanced NF-κB signaling [32]. Furthermore, genetic deletion of the mTOR kinase in hematopoietic stem cells resulted in NF-κB activation [51]. Our new observations are in line with those previously published. The molecular basis for these findings remained largely elusive until the Superti-Furga laboratory displayed that mTOR inhibition (via Torin-1 or PP242) markedly suppressed the re-synthesis of IκBα, resulting in enhanced nuclear abundance of p65 and, ultimately, expression of NF-κB target genes upon TNF-α stimulation [52]. As TNF-α is of pivotal importance in the early stages of liver regeneration [53], this mechanism could explain the enhanced NF-κB signaling observed by us. However, the exact molecular nature of

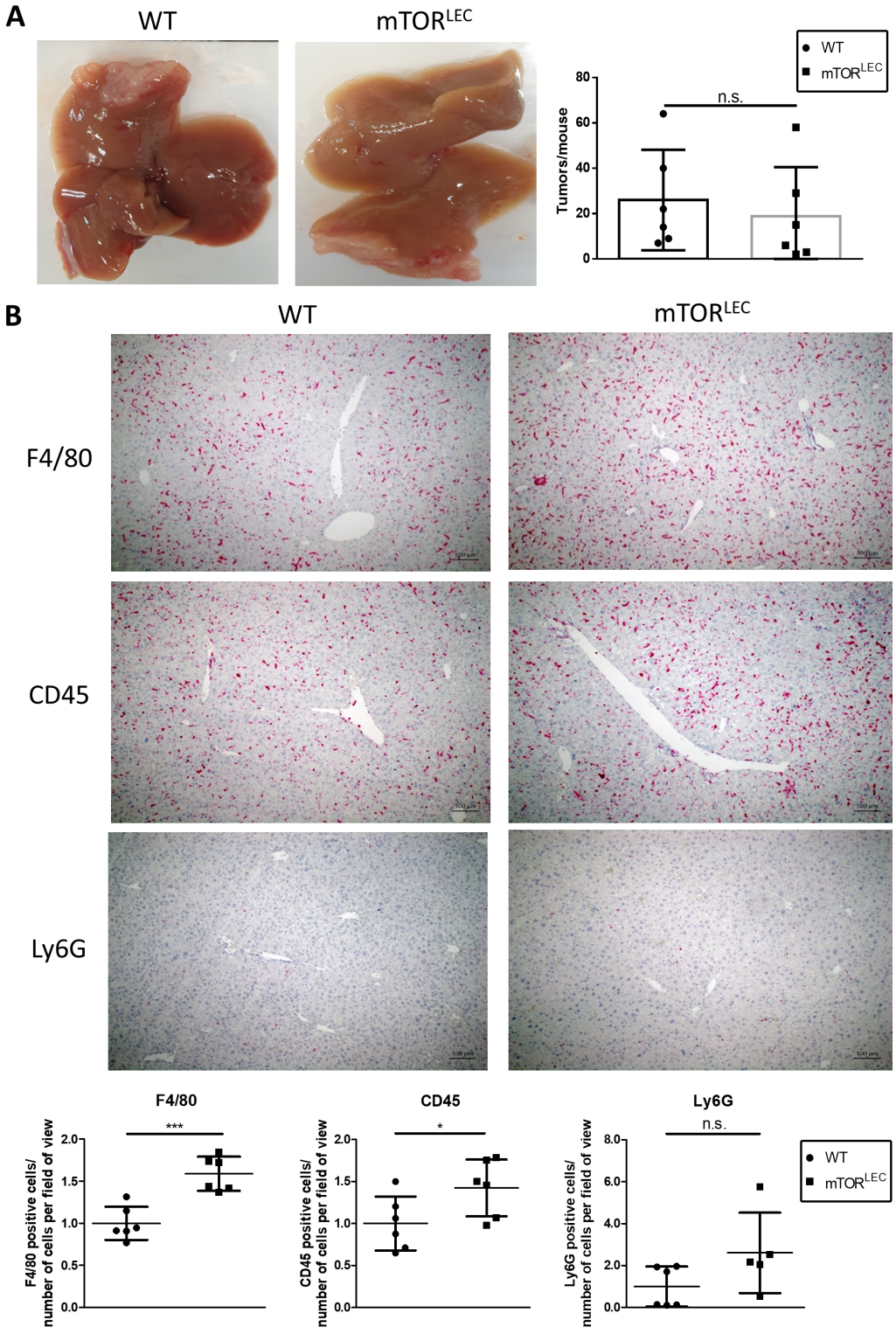

Figure 3. Loss of mTOR in LECs does not affect murine colon cancer liver metastasis. (A) Gross appearance of livers with MC38 metastases. Numbers of tumors in WT and mTOR^{LEC} mice were counted using ImageJ software and shown as bar charts. (B) The abundance of leukocytes (CD45), F4/80+ macrophages, and neutrophils (Ly6G) was investigated using IHC. Positive cells were counted using ImageJ, normalized to number of cells per field of view and shown as bar charts. Mean ± SEM, statistically analyzed using unpaired two-sided Student's *t*-test, $^{*}p < 0.05$, $^{***}p < 0.001$.

the interconnection of mTOR and NF-κB after partial liver resection remains elusive at this point and needs to be addressed by future work.

The association of increased metastasis with elevated canonical NF-κB signaling upon LEC-specific loss of mTOR suggested a functional importance of NF-κB for liver metastasis. This is in line with published work demonstrating reduced liver metastasis of murine lung cancer and melanoma due to functional inactivation of IKK-β, a kinase of pivotal importance for activation

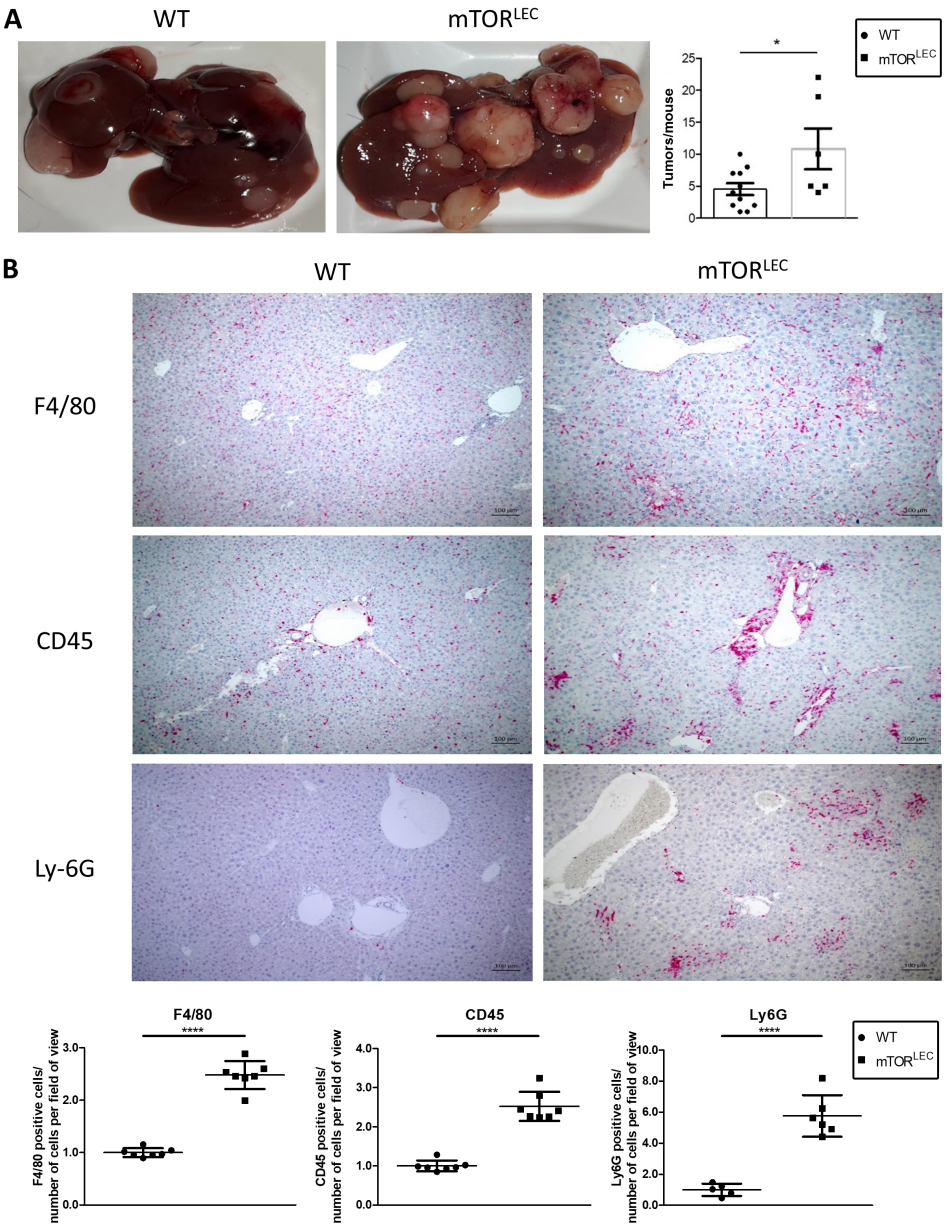

Figure 4. Enhanced metastatic load and inflammation after partial hepatectomy upon LEC-specific mTOR deletion. (A) Gross appearance of livers with MC38 metastases after partial hepatectomy. Numbers of tumors in WT and mTOR^{LEC} mice were counted using ImageJ software and shown as bar charts. (B) The abundance of leukocytes (CD45), F4/80+ macrophages, and neutrophils (Ly6G) was investigated using IHC. Positive cells were counted using ImageJ, normalized to number of cells per field of view and shown as bar charts. Mean ± SEM, statistically analyzed using unpaired two-sided Student's *t*-test, ***$p < 0.001$.

of the canonical NF-κB pathway [54]. In this publication, the authors were able to show activated canonical NF-κB signaling in murine livers in response to the establishment of metastases from Lewis lung carcinoma cells. Double staining for F4/80 and phospho-IκBα (an established marker of NF-kB activation) demonstrated that the majority of activated NF-κB was found in hepatic macrophages [54]. A functional importance of NF-κB in macrophages for metastatic growth was further supported by conditional gene targeting of IKK-β. Of note, LEC-specific deletion of IKK-β had no impact on the metastatic load in that publication [54]. The obvious conflict of our results with the work of Maeda *et al* [54] is probably explained by the different experimental set-ups. We only observed activation of the canonical NF-κB pathway in hepatocytes under conditions of mTOR deficiency and liver regeneration. Taken together, our data suggest that under certain conditions, the canonical NF-κB pathway in hepatocytes is indeed able to impact on the progression of liver metastases. It has to be stressed that our experimental set-up is not able to prove a causal link between enhanced NF-κB activity and acceleration of liver metastasis. This intriguing point is being addressed by current work in our group.

The PI3K/Akt/mTOR signaling pathway is activated by various growth factors and mitogens during the process of liver regeneration [55]. Successful and timely completion of liver regeneration after liver surgery is

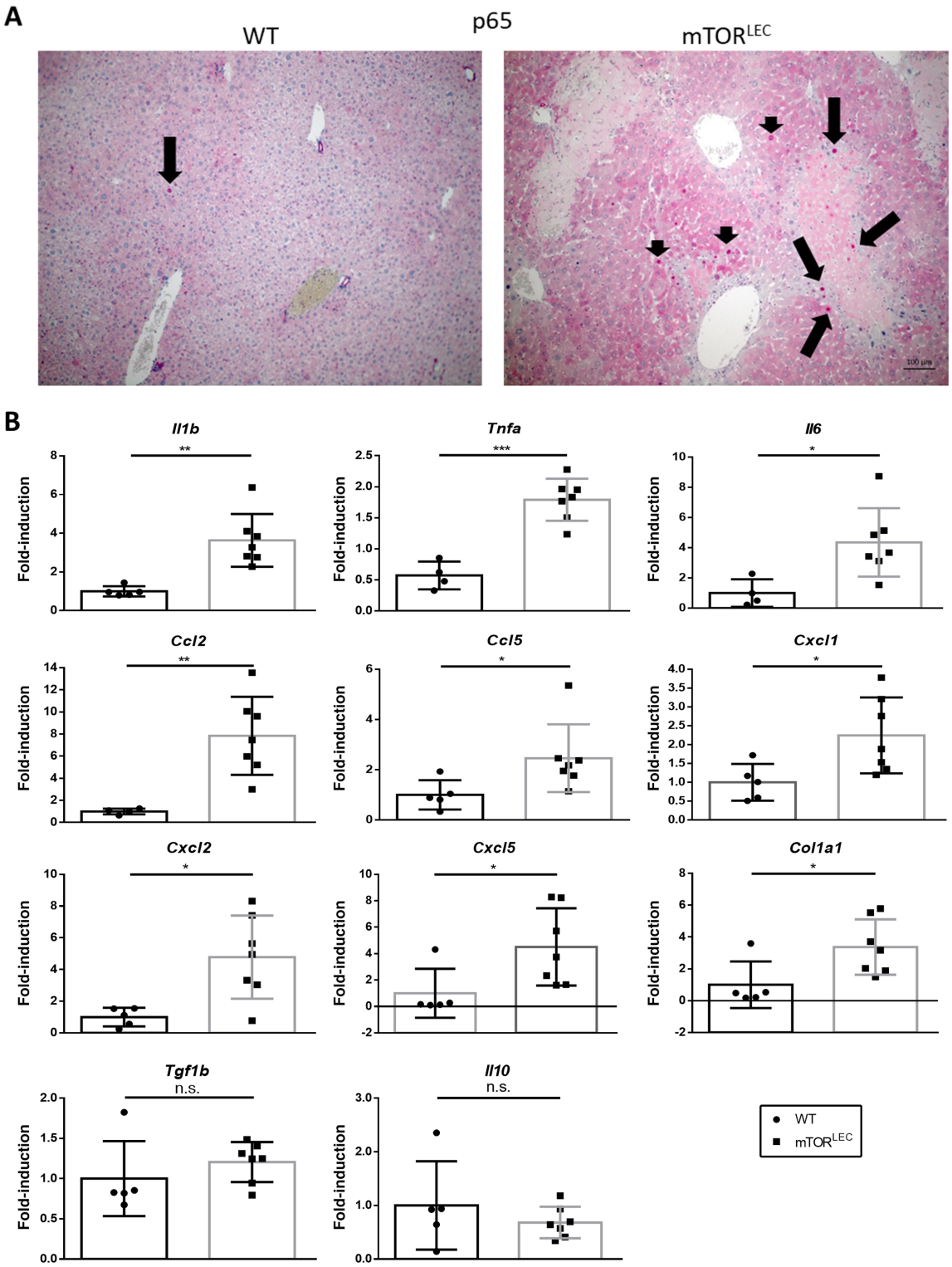

Figure 5. Elevated activity of the canonical NF-κB pathway in liver samples of mTOR^{LEC} mice after partial hepatectomy. (A) IHC for p65 revealed that canonical NF-κB activation is a rare event in hepatocytes without partial liver resection (left, arrow), whereas in the context of liver regeneration (right) nuclear p65 was found more frequently, both adjacent to (arrows) and distant from (arrowheads) focal necrotic areas. (B) Gene expression of established NF-κB target genes was determined using RT-qPCR, data were analyzed using qBase plus and the results shown as bar charts (KO relative to WT). Interleukin-1β (*Il1b*), Tumor necrosis factor-α (*Tnfa*), Interleukin-6 (*Il6*), Chemokine (C-C motif) ligand 2 (*Ccl2*), Chemokine(C-C motif) ligand 5 (*Ccl5*), Chemokine (C-X-C motif) ligand 1(*Cxcl1*), Chemokine (C-X-C motif) ligand 2 (*Cxcl2*), Chemokine (C-X-C motif) ligand 5 (*Cxcl5*) and Collagen type I alpha 1 (*Col1a1*) were all found significantly elevated in mTORLEC samples, while Transforming growth factor- β1(*Tgfb1*) and Interleukin-10 (*Il10*) are not significantly different. Mean ± SEM statistically analyzed by unpaired two-sided Student's *t* test, **p* < 0.05, ***p* <0.01, ****p* <0.001.

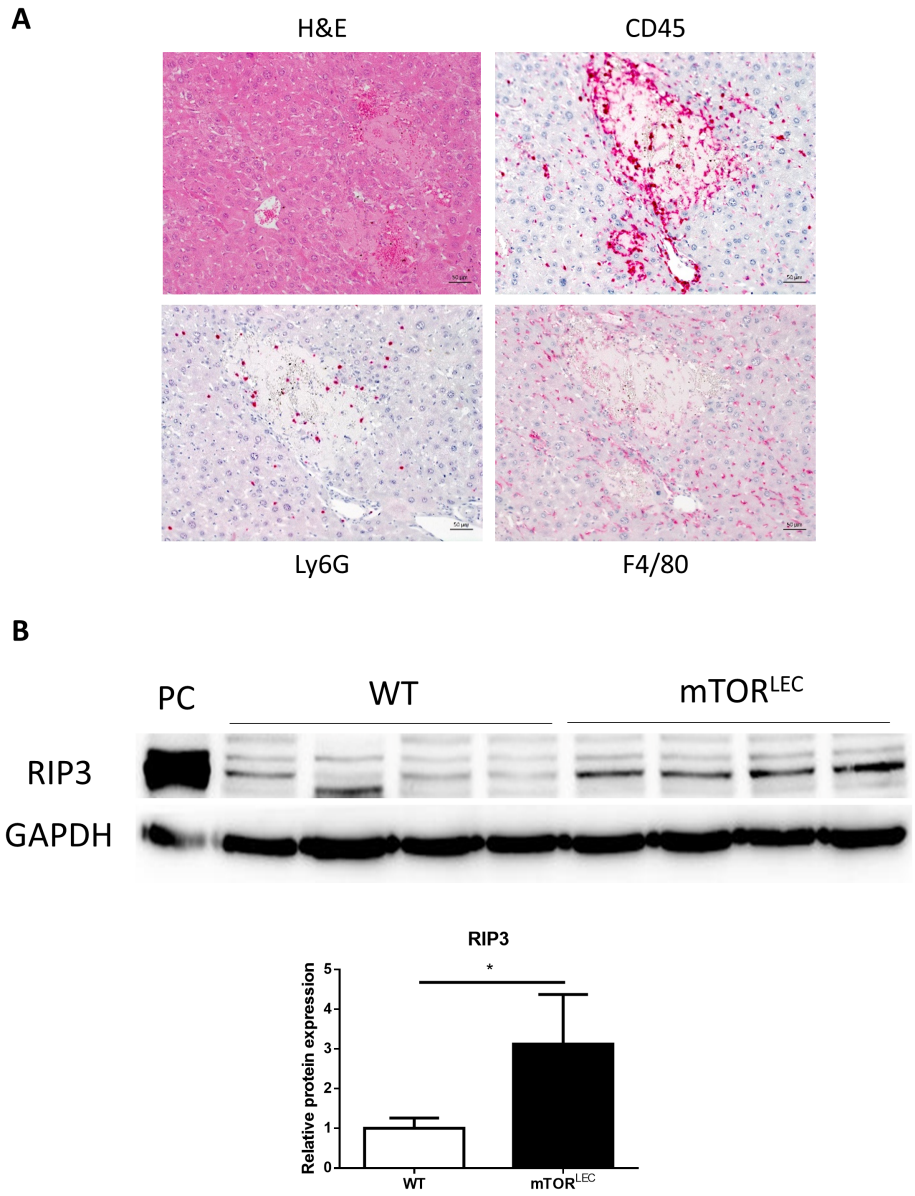

Figure 6. Development of necroptosis in the livers of mTOR^{LEC} mice during liver regeneration. (A) Morphology of focal necrotic areas in mTOR^{LEC} mice after partial hepatectomy. Sections were stained with H&E or antibodies against CD45, F4/80, and Ly6G. (B) Protein expression of the necroptosis marker RIP3K was analyzed by immunoblotting of whole liver lysates of WT and mTOR^{LEC} mice after partial hepatectomy. A sample from dextran sodium sulfate (DSS)-induced colitis served as the positive control (PC) and GAPDH as a loading control. Mean ± SEM, statistically analyzed using unpaired two-sided Student's *t*-test, $^{*}p < 0.05$.

of paramount importance for postoperative rehabilitation and the overall prognosis of the patient. Independent research groups were able to show that treatment with rapamycin and rapalogs did not significantly delay liver regeneration in different rodent models of partial hepatectomy [56–58]. Of note, the systemic administration of mTORC1 inhibitors was not without effect, as it significantly reduced hepatocyte proliferation, enhanced apoptosis of hepatic cells, and reduced expression of growth factors at different time points in the first week after partial hepatectomy [56–58]. However, this did not affect the timely completion of the regenerative process or the survival of the animals in a significant way. In principle, these results were confirmed in a mouse model displaying defective mTORC1 specifically in LECs [50]. Again, mTORC1 deficiency resulted in early defects of hepatocyte mitosis and enhanced hepatocellular damage early after partial liver resection, but overall liver regeneration and animal survival was not affected. Although these results argue for a compensable role of mTORC1 for liver regeneration, a different picture emerges when mTORC2 signaling is analyzed. Mice harboring a LEC-specific inactivation of mTORC2 (due to Cre/loxP-mediated deletion of *Rictor*) showed higher mortality after partial hepatectomy, potentially due to reduced activation of Akt [59]. These results suggest that the two basic components of mTOR encompass different functional roles for successful liver regeneration after partial hepatectomy. Our results are seemingly not in line with this suggestion as we did not observe defective liver regeneration upon LEC-specific inactivation of the mTOR kinase (resulting in the loss of both

mTORC1 and mTORC2). Of note, our mouse model is characterized by a rather low KO efficiency, much lower compared to the efficiency reported for albumin-Cre-driven deletion of *Raptor* and *Rictor*, respectively [50,60]. This points to a paramount importance of mTOR signaling for the function and survival of hepatocytes and bile duct epithelial cells. It can be concluded that the low KO efficiency observed in our mice explains the inconsistency with the work of Xu *et al* [59], who have noted a significant contribution of mTORC2 in LECs for regeneration after partial hepatectomy.

Necroptosis is a form of programmed cell death and a characteristic response of caspase-8-deficient cells to TNF-α or other stimulators of the extrinsic pathway of triggering apoptosis [41,61,62]. We observed necroptosis in $mTOR^{LEC}$ mice after partial hepatectomy in a situation of enhanced activity of the canonical NF-κB pathway. This conflicts with reports demonstrating necroptosis in mice with robustly reduced NF-κB activity in LECs due to deletion of IKKα/β or TGF-β-activated kinase 1 (TAK-1) [42,63]. Of note, our experimental set-up did not permit us to unravel the exact functional connection between necroptosis and enhanced NF-κB activity. Although the results mentioned above support a necroptosis-inhibiting role for NF-κB reminiscent of the well-established anti-apoptotic function of NF-κB, our observations could be explained by an activation of the canonical NF-κB pathway downstream of necroptosis. In fact, this is supported by published data from the group of Junying Yuan [64] (who coined the term 'necroptosis' in 2005), demonstrating robust activation of the canonical NF-κB pathway in various cell lines in response to activation of necroptosis. What is more, the group of Yuan reported enhanced expression and secretion of proinflammatory cytokines as a consequence of necroptosis-induced NF-κB activation, in line with our results. Taken together, this suggested that the LEC-specific inactivation of mTOR results in the activation of hepatocellular necroptosis in the context of liver regeneration due to partial hepatectomy. However, this is not supported by the published literature, where several independent groups have reported a functional importance of mTOR activation for the execution of necroptosis [65–67]. We cannot rule out the possibility that the focal necrotic areas in the $mTOR^{LEC}$ mice originated from mTOR-proficient hepatocytes. It is at least conceivable that the intercellular communication in the liver is modified by the presence of mTOR-deficient hepatocytes in such a way that a regenerative stimulus results in focal necroptosis. Although this seems to be a rather daring hypothesis, cell-intrinsic effects of the mTOR loss might be better suited to explain our observation. Specifically, a potential impact of the loss of mTOR on the activity of caspase-8 should be addressed.

Acknowledgements

Research in the Cramer laboratory was supported by grants from the Deutsche Forschungsgemeinschaft (CR 133/2-1 until 2-4 and CR 133/3-1). LJ was supported by the China Scholarship Council (CSC, file no. 201706260268). The excellent technical assistance of Nelli Neuberger and Ilka Sauer is highly appreciated. We are grateful to Pavel Strnad (Gastroenterology, RWTH Aachen University Hospital) for helpful discussions and for providing control reagents. This work was presented in part as a short talk at the 2019 United European Gastroenterology Week in Barcelona, Spain.

Author contributions statement

LJ, RE, MS, UPN and TC conceptualized the study. LJ, RE, SJ, JR, AE, ME, HD, CL-I and LRH performed experiments. LJ, RE, SJ, AE, ME, HD, CL-I, DM, LRH and TC analyzed and visualized data. LJ, RE, AE and TC wrote and revised the manuscript. UPN and TC supervised the study and acquired funding. Project administration was performed by TC. All authors have seen and approved the revised manuscript.

Data availability statement

The MS data have been deposited with the ProteomeXchange Consortium (http://proteomecentral.proteomexchange.org) via the PRIDE partner repository [27] with the dataset identifier PXD019998.

References

1. Mattiuzzi C, Sanchis-Gomar F, Lippi G. Concise update on colorectal cancer epidemiology. *Ann Transl Med* 2019; **7:** 609.
2. Siegel RL, Miller KD, Fedewa SA, *et al*. Colorectal cancer statistics, 2017. *CA Cancer J Clin* 2017; **67:** 177–193.
3. Zarour LR, Anand S, Billingsley KG, *et al*. Colorectal cancer liver metastasis: evolving paradigms and future directions. *Cell Mol Gastroenterol Hepatol* 2017; **3:** 163–173.
4. Dhir M, Sasson AR. Surgical management of liver metastases from colorectal cancer. *J Oncol Pract* 2016; **12:** 33–39.
5. Sceneay J, Smyth MJ, Möller A. The pre-metastatic niche: finding common ground. *Cancer Metastasis Rev* 2013; **32:** 449–464.
6. Beuth J, Ko HL, Oette K, *et al*. Inhibition of liver metastasis in mice by blocking hepatocyte lectins with arabinogalactan infusions and D-galactose. *J Cancer Res Clin Oncol* 1987; **113:** 51–55.
7. Long L, Nip J, Brodt P. Paracrine growth stimulation by hepatocyte-derived insulin-like growth factor-1: a regulatory mechanism for carcinoma cells metastatic to the liver. *Cancer Res* 1994; **54:** 3732–3737.
8. Lee JW, Stone ML, Porrett PM, *et al*. Hepatocytes direct the formation of a pro-metastatic niche in the liver. *Nature* 2019; **567:** 249–252.
9. Moya IM, Castaldo SA, Van den Mooter L, *et al*. Peritumoral activation of the Hippo pathway effectors YAP and TAZ suppresses liver cancer in mice. *Science* 2019; **366:** 1029–1034.
10. DeBerardinis RJ, Chandel NS. Fundamentals of cancer metabolism. *Sci Adv* 2016; **2:** e1600200.
11. Elia I, Doglioni G, Fendt SM. Metabolic hallmarks of metastasis formation. *Trends Cell Biol* 2018; **28:** 673–684.
12. Elia I, Fendt S-M. *In vivo* cancer metabolism is defined by the nutrient microenvironment. *Transl Cancer Res* 2016; **5:** S1284–S1287.

13. Christen S, Lorendeau D, Schmieder R, *et al*. Breast cancer-derived lung metastases show increased pyruvate carboxylase-dependent anaplerosis. *Cell Rep* 2016; **17:** 837–848.
14. Loo JM, Scherl A, Nguyen A, *et al*. Extracellular metabolic energetics can promote cancer progression. *Cell* 2015; **160:** 393–406.
15. Albert V, Hall MN. mTOR signaling in cellular and organismal energetics. *Curr Opin Cell Biol* 2015; **33:** 55–66.
16. Cornu M, Albert V, Hall MN. mTOR in aging, metabolism, and cancer. *Curr Opin Genet Dev* 2013; **23:** 53–62.
17. Ricoult SJ, Manning BD. The multifaceted role of mTORC1 in the control of lipid metabolism. *EMBO Rep* 2013; **14:** 242–251.
18. Ni HM, Chao X, Yang H, *et al*. Dual roles of mammalian target of rapamycin in regulating liver injury and tumorigenesis in autophagy-defective mouse liver. *Hepatology* 2019; **70:** 2142–2155.
19. Kos CH. Cre/loxP system for generating tissue-specific knockout mouse models. *Nutr Rev* 2004; **62:** 243–246.
20. Gangloff YG, Mueller M, Dann SG, *et al*. Disruption of the mouse mTOR gene leads to early postimplantation lethality and prohibits embryonic stem cell development. *Mol Cell Biol* 2004; **24:** 9508–9516.
21. Postic C, Shiota M, Niswender KD, *et al*. Dual roles for glucokinase in glucose homeostasis as determined by liver and pancreatic beta cell-specific gene knock-outs using Cre recombinase. *J Biol Chem* 1999; **274:** 305–315.
22. Corbett TH, Griswold DP Jr, Roberts BJ, *et al*. Tumor induction relationships in development of transplantable cancers of the colon in mice for chemotherapy assays, with a note on carcinogen structure. *Cancer Res* 1975; **35:** 2434–2439.
23. Berndt N, Egners A, Mastrobuoni G, *et al*. Kinetic modelling of quantitative proteome data predicts metabolic reprogramming of liver cancer. *Br J Cancer* 2020; **122:** 233–244.
24. Hori T, Ohashi N, Chen F, *et al*. Simple and reproducible hepatectomy in the mouse using the clip technique. *World J Gastroenterol* 2012; **18:** 2767–2774.
25. Ramakers C, Ruijter JM, Deprez RH, *et al*. Assumption-free analysis of quantitative real-time polymerase chain reaction (PCR) data. *Neurosci Lett* 2003; **339:** 62–66.
26. Pfaffl MW. A new mathematical model for relative quantification in real-time RT-PCR. *Nucleic Acids Res* 2001; **29:** e45.
27. Martens L, Hermjakob H, Jones P, *et al*. PRIDE: the proteomics identifications database. *Proteomics* 2005; **5:** 3537–3545.
28. Subramanian A, Tamayo P, Mootha VK, *et al*. Gene set enrichment analysis: a knowledge-based approach for interpreting genome-wide expression profiles. *Proc Natl Acad Sci U S A* 2005; **102:** 15545–15550.
29. Shan T, Zhang P, Jiang Q, *et al*. Adipocyte-specific deletion of mTOR inhibits adipose tissue development and causes insulin resistance in mice. *Diabetologia* 2016; **59:** 1995–2004.
30. Liu GY, Sabatini DM. mTOR at the nexus of nutrition, growth, ageing and disease. *Nat Rev Mol Cell Biol* 2020; **21:** 183–203.
31. Heymann F, Tacke F. Immunology in the liver–from homeostasis to disease. *Nat Rev Gastroenterol Hepatol* 2016; **13:** 88–110.
32. Weichhart T, Costantino G, Poglitsch M, *et al*. The TSC-mTOR signaling pathway regulates the innate inflammatory response. *Immunity* 2008; **29:** 565–577.
33. Yang CS, Song CH, Lee JS, *et al*. Intracellular network of phosphatidylinositol 3-kinase, mammalian target of the rapamycin/70 kDa ribosomal S6 kinase 1, and mitogen-activated protein kinases pathways for regulating mycobacteria-induced IL-23 expression in human macrophages. *Cell Microbiol* 2006; **8:** 1158–1171.
34. Schmitz F, Heit A, Dreher S, *et al*. Mammalian target of rapamycin (mTOR) orchestrates the defense program of innate immune cells. *Eur J Immunol* 2008; **38:** 2981–2992.
35. Ganley IG, Lam Du H, Wang J, *et al*. ULK1.ATG13.FIP200 complex mediates mTOR signaling and is essential for autophagy. *J Biol Chem* 2009; **284:** 12297–12305.
36. Blommaart EF, Luiken JJ, Blommaart PJ, *et al*. Phosphorylation of ribosomal protein S6 is inhibitory for autophagy in isolated rat hepatocytes. *J Biol Chem* 1995; **270:** 2320–2326.
37. Noda T, Ohsumi Y. Tor, a phosphatidylinositol kinase homologue, controls autophagy in yeast. *J Biol Chem* 1998; **273:** 3963–3966.
38. Lafreniere R, Rosenberg SA. A novel approach to the generation and identification of experimental hepatic metastases in a murine model. *J Natl Cancer Inst* 1986; **76:** 309–322.
39. Taniguchi K, Karin M. NF-κB, inflammation, immunity and cancer: coming of age. *Nat Rev Immunol* 2018; **18:** 309–324.
40. Ghosh S, Tergaonkar V, Rothlin CV, *et al*. Essential role of tuberous sclerosis genes TSC1 and TSC2 in NF-kappaB activation and cell survival. *Cancer Cell* 2006; **10:** 215–226.
41. Degterev A, Huang Z, Boyce M, *et al*. Chemical inhibitor of nonapoptotic cell death with therapeutic potential for ischemic brain injury. *Nat Chem Biol* 2005; **1:** 112–119.
42. Vucur M, Reisinger F, Gautheron J, *et al*. RIP3 inhibits inflammatory hepatocarcinogenesis but promotes cholestasis by controlling caspase-8- and JNK-dependent compensatory cell proliferation. *Cell Rep* 2013; **4:** 776–790.
43. Zhang DW, Shao J, Lin J, *et al*. RIP3, an energy metabolism regulator that switches TNF-induced cell death from apoptosis to necrosis. *Science* 2009; **325:** 332–336.
44. Schwabe RF, Luedde T. Apoptosis and necroptosis in the liver: a matter of life and death. *Nat Rev Gastroenterol Hepatol* 2018; **15:** 738–752.
45. Li Z, Zhang J, Mulholland M, *et al*. mTOR activation protects liver from ischemia/reperfusion-induced injury through NF-kappaB pathway. *FASEB J* 2017; **31:** 3018–3026.
46. Liu Y, Zhang Y, Li T, *et al*. The tight junction protein TJP1 regulates the feeding-modulated hepatic circadian clock. *Nat Commun* 2020; **11:** 589.
47. Lamming DW, Ye L, Katajisto P, *et al*. Rapamycin-induced insulin resistance is mediated by mTORC2 loss and uncoupled from longevity. *Science* 2012; **335:** 1638–1643.
48. Champion L, Stern M, Israël-Biet D, *et al*. Brief communication: sirolimus-associated pneumonitis: 24 cases in renal transplant recipients. *Ann Intern Med* 2006; **144:** 505–509.
49. Thaunat O, Beaumont C, Chatenoud L, *et al*. Anemia after late introduction of sirolimus may correlate with biochemical evidence of a chronic inflammatory state. *Transplantation* 2005; **80:** 1212–1219.
50. Umemura A, Park EJ, Taniguchi K, *et al*. Liver damage, inflammation, and enhanced tumorigenesis after persistent mTORC1 inhibition. *Cell Metab* 2014; **20:** 133–144.
51. Guo F, Li J, Du W, *et al*. mTOR regulates DNA damage response through NF-κB-mediated FANCD2 pathway in hematopoietic cells. *Leukemia* 2013; **27:** 2040–2046.
52. Karonitsch T, Kandasamy RK, Kartnig F, *et al*. mTOR senses environmental cues to shape the fibroblast-like synoviocyte response to inflammation. *Cell Rep* 2018; **23:** 2157–2167.
53. Forbes SJ, Newsome PN. Liver regeneration - mechanisms and models to clinical application. *Nat Rev Gastroenterol Hepatol* 2016; **13:** 473–485.
54. Maeda S, Hikiba Y, Sakamoto K, *et al*. Ikappa B kinasebeta/nuclear factor-kappaB activation controls the development of liver metastasis by way of interleukin-6 expression. *Hepatology* 2009; **50:** 1851–1860.
55. Wei X, Luo L, Chen J. Roles of mTOR signaling in tissue regeneration. *Cells* 2019; **8:** 1075.
56. Dahmen U, Gu Y, Shen K, *et al*. Onset of liver regeneration after subtotal resection is inhibited by the use of new immunosuppressive drugs. *Transplant Proc* 2002; **34:** 2312–2313.
57. Fouraschen SM, de Ruiter PE, Kwekkeboom J, *et al*. mTOR signaling in liver regeneration: rapamycin combined with growth factor treatment. *World J Transplant* 2013; **3:** 36–47.

58. Palmes D, Zibert A, Budny T, *et al*. Impact of rapamycin on liver regeneration. *Virchows Arch* 2008; **452:** 545–557.
59. Xu M, Wang H, Wang J, *et al*. mTORC2 signaling is necessary for timely liver regeneration after partial hepatectomy. *Am J Pathol* 2020; **190:** 817–829.
60. Hagiwara A, Cornu M, Cybulski N, *et al*. Hepatic mTORC2 activates glycolysis and lipogenesis through Akt, glucokinase, and SREBP1c. *Cell Metab* 2012; **15:** 725–738.
61. Holler N, Zaru R, Micheau O, *et al*. Fas triggers an alternative, caspase-8-independent cell death pathway using the kinase RIP as effector molecule. *Nat Immunol* 2000; **1:** 489–495.
62. Vercammen D, Beyaert R, Denecker G, *et al*. Inhibition of caspases increases the sensitivity of L929 cells to necrosis mediated by tumor necrosis factor. *J Exp Med* 1998; **187:** 1477–1485.
63. Koppe C, Verheugd P, Gautheron J, *et al*. IκB kinaseα/β control biliary homeostasis and hepatocarcinogenesis in mice by phosphorylating the cell-death mediator receptor-interacting protein kinase 1. *Hepatology* 2016; **64:** 1217–1231.
64. Zhu K, Liang W, Ma Z, *et al*. Necroptosis promotes cell-autonomous activation of proinflammatory cytokine gene expression. *Cell Death Dis* 2018; **9:** 500.
65. Abe K, Yano T, Tanno M, *et al*. mTORC1 inhibition attenuates necroptosis through RIP1 inhibition-mediated TFEB activation. *Biochim Biophys Acta Mol Basis Dis* 2019; **1865:** 165552.
66. Liu Q, Qiu J, Liang M, *et al*. Akt and mTOR mediate programmed necrosis in neurons. *Cell Death Dis* 2014; **5:** e1084.
67. Xie Y, Zhao Y, Shi L, *et al*. Gut epithelial TSC1/mTOR controls RIPK3-dependent necroptosis in intestinal inflammation and cancer. *J Clin Invest* 2020; **130:** 2111–2128.

SUPPLEMENTARY MATERIAL ONLINE

Figure S1. GP73 immunohistochemistry

Figure S2. PCR and western blot analyses of hepatocytes from WT and mTOR^{LEC} mice

Figure S3. Analysis of liver proteomes

Figure S4. STRING PPI (protein–protein interaction) network and pathway analysis of proteins with downregulation at least one standard deviation from the log2 transformed median values in mTOR^{LEC}/WT liver tissue

Figure S5. Representative H&E staining of livers of WT and mTOR^{LEC} mice and analyses of cell size

Figure S6. Effect of LEC-specific mTOR deletion on proliferation and apoptosis of hepatocytes

Figure S7. Gene expression was determined using RT-qPCR

Figure S8. Analysis of autophagy in WT and mTOR^{LEC} livers

Figure S9. Proliferation of tumor cells and hepatocytes adjacent to metastases was analyzed using immunohistochemistry for phosphorylated Histone H3

Figure S10. Schematic diagram of the mouse models of colon cancer (MC38 cells) liver metastases used

Figure S11. Proliferation of tumor cells and hepatocytes adjacent to metastases after partial hepatectomy was analyzed using immunohistochemistry for phosphorylated Histone H3

Figure S12. Quantification of immunohistochemistry for p65 from Figure 5A

Figure S13. Further examples of the histomorphology and quantification of necroptotic areas in mTOR^{LEC} livers after partial liver resection

Figure S14. Graphical summary demonstrating the potential sequence of events leading to enhanced metastatic growth after partial liver resection upon LEC-specific mTOR loss

Table S1. Sequences of primers used for RT-qPCR